sciendo

POLISH MARITIME RESEARCH 1 (105) 2020 Vol. 27; pp. 6-17
10.2478/pomr-2020-0001

PROPELLER HYDRODYNAMIC CHARACTERISTICS IN OBLIQUE FLOW BY UNSTEADY RANSE SOLVER

Hossein Nouroozi
Hamid Zeraatgar
Amirkabir University of Technology, Tehran, Iran

ABSTRACT

Propellers may encounter oblique flow during operation in off-design conditions. Study of this issue is important from the design and ship performance points of view. On the other hand, a propeller operating in oblique flow may sometimes result in a better propulsion efficiency. The main goal of the present study is to provide an insight on the propeller characteristics in the oblique flow condition. In this research, the performance of the DTMB 4419 propeller is studied by the numerical method based on solving Reynolds Averaged Navier–Stokes (RANS) equations in several inflow angles. The sliding mesh approach is used to model the rotary motion of the propeller. Initially, the numerical method is verified by grid and time step dependency analysis at various inflow angles. Additionally, computed results at zero inflow angle are compared with the available experimental data and good agreement is achieved. Finally, the forces and moments acting on the propeller are obtained for 0° to 30° inflow angles. It is concluded that the inflow angle up to 10° has no significant influence on the thrust and torque coefficients as well as the propeller efficiency. However, at high angles up to 30°, the thrust and torque coefficients increase as the inflow angle increases, which may result in a significant improvement of propeller efficiency.

Keywords: DTMB-P4119 propeller, URANS equation, oblique flow, sliding mesh technique

INTRODUCTION

Ship propellers are mounted symmetrically behind ships and the dominant inflow is axial. So, propeller performance is evaluated in a straight path of constant forward speed in a calm water condition. Propeller design is intended to achieve maximum efficiency for the required thrust, using conventional propeller geometry available by regression methods. The blade sections are located in such a way as to have the highest lift-to-drag ratio at the design speed at an appropriate angle of attack with respect to the axial inflow.

In the straight path condition, a vessel's wake flow field is composed of velocity components in the axial, radial and tangential directions, where the radial and tangential components are significantly smaller than the axial component. The radial and tangential velocities components are in the propeller plane and may be called in-plane components. It is worth mentioning that the in-plane component around the propeller disc is symmetric.

However, during their lifetime, ships may experience conditions other than straight paths, such as turning manoeuvres, operating in rough seas, and so on. During ship manoeuvring, such as a turning manoeuvre, the in-plane velocity component increases considerably relative to the axial component. Furthermore, in the turning manoeuvre, the propeller faces an asymmetric or oblique flow. The in-plane component of the oblique flow causes a different angle of attack of each blade. Therefore, the summations of hydrodynamic loads of blades are no longer symmetric.

In the case of symmetric flow, thrust force is the only load generated by the propeller. As far as the asymmetric condition is concerned, transverse and vertical forces are also generated

in addition to the thrust force. Although the transverse and vertical forces disturb the mechanical system of ships, it has been claimed that the propeller efficiency may increase at oblique flow in certain conditions.

Numerous numerical and experimental researches have been carried out to study propeller characteristics in open water. In most studies, a propeller in axial symmetric flow has been investigated. Viviani et al.[26] conducted a study on a twin-screw vessel. They showed that, during the turning manoeuvre, the propeller power/torque ratio increases in respect to the straight path, by up to 50% and 100% for the internal and external propellers (relative to the centre of rotation), respectively. Atsavapranee et al. [2] proved that the vertical and transverse forces generated by the propeller during oblique flow might strongly influence the dynamic response (path stability and turning quality) of the craft based on the test results. Durante et al. [12] utilised a hybrid model with promising results, including an actuator disc for considering the axial flow component and Ribner's lateral force model [22] to account for transverse flow effects. They emphasised the need for a propeller lateral force model to estimate the complex phenomena related to oblique flow. Broglia et al. [3] carried out a numerical calculation on a twin-screw model with a single rudder using the unsteady RANS solver. Several propeller models have been investigated in order to consider the effect of oblique flow components occurring during the turning manoeuvre. The main features of the flow as well as vertical structures detached from the hull were studied.

In recent years, numerical methods based on solution of the RANS equations have been significantly improved and widely used to solve marine hydrodynamic issues. As an example, Hochbaum [13] predicted the manoeuvring of a ship based on the determination of hydrodynamic derivatives using a virtual PMM test (in the software environment). A similar study was carried out by Simonsen et al. [25] to perform the IMO standard deep water manoeuvring simulation for a model ship in which hydrodynamic coefficients were calculated by a combination of the RANS method and measurement.

Krasilnikov et al. [16] studied the blade forces for a podded propeller in pulling and pushing modes in oblique flow through the solution of unsteady RANS equations. Based on the analysis of the results, they concluded that the blades in pulling mode encounter considerable force at positive and negative inflow angles, which are influenced by the lateral flow. Dubbioso et al. [7] investigated the turning manoeuvre performance of a twin-propeller ship using model tests and numerical simulations. The results indicate that during vessel turning, the wake flow has an asymmetric distribution, which causes different oblique flows to be imposed on the propellers. Coraddu et al. [6] showed that, during a hard manoeuvre, the propeller torque increases by more than 100% relative to steady motion. Shamsi and Ghassemi [23, 24] studied the effects of the inflow angle on the characteristics of a podded propulsor and a DTMB propeller. In these researches, using the RANS solver along with a moving reference frame (MRF) and the sliding mesh method, they showed that the hydrodynamic loads depend on the advance coefficients and inflow angles, and in the non-symmetric flow, the propeller generates significant forces and moments.

Abbasi et al. [1] studied the hydrodynamic characteristics of a B-Series propeller (B:4-70) in oblique flow using the RANS solver of the StarCCM+ software. They claimed that the propeller thrust and torque coefficients are reduced by increasing the inflow angle and the advance coefficient. Dubbioso et al. [8, 9], using the dynamic overlapping grid technique and an in-house CFD solver, studied the performance of the INSEAN E779A model propeller in the oblique flow condition. Numerical calculations were carried out for two advance ratios, and two inflow angles, and blades forces and flow characteristics were obtained. The results of the open water propeller performance in the axial flow are in good agreement with the experiment, but the results are not evaluated in oblique flow due to a lack of experimental data. Yao [28] calculated the hydrodynamic performance of a propeller using the RANS solver of Open FOAM software. The sliding mesh technique is used to model the propeller's rotary motion. The results have an acceptable agreement with the experimental data. Ortolani et al. [19, 20] conducted studies on the propeller's transverse and vertical forces for a twin-screw ship by means of free running model tests. For the same model, Dubbioso et al. [10] performed numerical studies to examine the characteristics of the forces generated by the propeller in the oblique flow condition during a turning manoeuvre.

As reviewed above, sea trials have shown that during turning manoeuvres, the propeller power/torque demand significantly increases in respect to a straight path. Consideration of the propeller loads in the oblique flow condition is crucial to develop an appropriate control system to prevent structural damage [6]. Therefore, investigation of the propeller performance at oblique inflow angles is of paramount importance to improve the propeller sizing and design. Furthermore, reliable prediction of relevant loads on the propeller exerted during manoeuvres is essential to provide an accurate estimation of the vessel's dynamic response.

Moreover, oblique inflow may have a capability for propeller efficiency improvement if used as a tool for ship fuel consumption reduction. Based on the above consideration, the hydrodynamic characteristics of the DTMB-P4119 propeller at different inflow angles up to 30° are calculated using the numerical simulation of unsteady RANS equations.

Computations for the DTMB-P4119 model were carried out in symmetric flow using the commercial CFD software, FLUENT R14.5, and validated by the available experimental data. The study continued in oblique flow conditions for inflow angles up to 30° where thrust, transverse and vertical forces in conjunction with propeller torque are calculated. The study shows that there is room for a considerable increase of propeller efficiency at high inflow angle.

GOVERNING EQUATIONS

The fluid flow governing equations, including the conservation equation for mass and momentum and Navier–Stokes equations, are written as follows:

$$\frac{\partial \rho}{\partial t} + \frac{\partial (\rho u_i)}{\partial x_i} = S_m \qquad i = 1, 2, 3 \tag{1}$$

where ρ is the water density, u_i is the ith velocity component, x_i is the ith coordinate axis and S_m is a source term. In the incompressible fluid flow around the propeller, density is considered to be constant. So, the mass continuity equation is modified as follows:

$$\frac{\partial u_i}{\partial x_i} = 0 \qquad i = 1, 2, 3 \tag{2}$$

The momentum conservation equation is expressed as:

$$\frac{\partial (\rho u_i)}{\partial t} + \frac{\partial (\rho u_i u_j)}{\partial x_j} = -\frac{\partial p}{\partial x_i} + \rho g_i + F_i + \frac{\partial \tau_{ij}}{\partial x_j} \qquad i = 1, 2, 3 \tag{3}$$

where p is the static pressure, g_i is a gravitational constant, F_i is body force components. The body force and are regarded as zero in the present research. Here τ_{ij} is the Reynolds stress tensor, which is calculated as below:

$$\tau_{ij} = \mu \left(\frac{\partial u_i}{\partial x_j} + \frac{\partial u_j}{\partial x_i} \right) - \frac{2}{3} \mu \frac{\partial u_l}{\partial x_l} \delta_{ij} \tag{4}$$

where μ is the dynamic viscosity coefficient and δ_{ij} is the Kronecker delta, which is equal to unity when $i = j$ and zero when $i \neq j$. The Reynolds averaged form of the momentum equation, including the turbulent shear stresses, is written as follows:

$$\frac{\partial}{\partial t}(\rho u_i) + \frac{\partial}{\partial x_j}(\rho u_i u_j) =$$

$$= \frac{\partial}{\partial x_j}\left[\mu \left(\frac{\partial u_i}{\partial x_j} + \frac{\partial u_j}{\partial x_i} \right) - \left(\frac{2}{3} \mu \frac{\partial u_i}{\partial x_i} \right) \right] - \frac{\partial p}{\partial x_i} + \frac{\partial}{\partial x_j}(-\rho \overline{\acute{u}_l \acute{u}_j}) \tag{5}$$

The last term on the right-hand side is related to the Reynolds stresses, in which $\acute{u}_l$ is the component of the instantaneous velocity in the ith direction. This term can be written, using Boussinesq's eddy viscosity hypothesis, as follows:

$$-\rho \overline{\acute{u}_l \acute{u}_j} = 2 \mu_t \bar{S}_{ij}$$

$$\bar{S}_{ij} = \frac{1}{2}\left(\frac{\partial u_i}{\partial x_j} + \frac{\partial u_j}{\partial x_i} \right) \tag{6}$$

where μ_t is the turbulence viscosity and $\bar{S}_{ij}$ is the average strain rate tensor. Therefore, by substituting the above expression equivalent to the Reynolds stress tensor, the momentum conservation equation, Eq. (3), changes as shown below:

$$\frac{\partial (\rho u_i)}{\partial t} + \frac{\partial (\rho u_i u_j)}{\partial x_j} = -\frac{\partial p}{\partial x_i} + \frac{\partial}{\partial x_j}[2(\mu + \mu_t) S_{ij}] \tag{7}$$

The above equations along with the continuity equation are called the Reynolds Averaged Navier–Stokes (RANS) equations. Eq. (5) is very similar to the laminar flow governing equation, Eq. (3). The only difference is in the diffusion term due to the existence of the turbulence viscosity. Therefore, in turbulent flow simulation, using the Boussinesq hypothesis, turbulence modelling is performed by calculating the turbulence viscosity coefficient (μ_t). To calculate the turbulence viscosity, the auxiliary equations of different turbulence models such as k-ε or k-ω can be employed. Assessment of the results of similar studies on the numerical simulation of flow around marine propellers such as [4, 17, 18, 21], regarding the influence of the various turbulence models on the precision of the propeller performance prediction, demonstrate the preference for the k-ω turbulence model relative to others. Therefore, this model, developed by Wilcox [27], is employed in this study. The equations of this model are as follows:

$$\frac{\partial (\rho k)}{\partial t} + \frac{\partial (\rho k u_i)}{\partial x_i} = \tau_{ij} \frac{\partial u_i}{\partial x_j} \rho \beta^* k \omega + \frac{\partial}{\partial x_i}\left[\left(\mu + \frac{\mu_t}{\sigma_k} \right) \frac{\partial k}{\partial x_j} \right]$$

$$\frac{\partial (\rho \omega)}{\partial t} + \frac{\partial (\rho \omega u_i)}{\partial x_i} = \frac{\alpha \omega}{k} \tau_{ij} \frac{\partial u_i}{\partial x_j} - \rho \beta \omega^2 + \frac{\partial}{\partial x_i}\left[\left(\mu + \frac{\mu_t}{\sigma_\omega} \right) \frac{\partial k}{\partial x_j} \right] \tag{8}$$

where k is the turbulence kinetic energy representing the velocity scale and ω is the turbulence dissipation rate which represents the length scale of turbulence. σ_k and σ_ω are the turbulent Prandtl numbers for k and ω, respectively. The turbulence viscosity is calculated by the following equation:

$$\mu_t = \frac{\rho k}{\omega} \tag{9}$$

CASE STUDY

PROPELLER MODEL

The P4119 David Taylor Model Basin's propeller model is selected for the study, for which experimental data is available in the open water condition for steady axial flow. The DTMB-P4119 is a three-bladed fixed-pitch propeller with diameter of D = 0.305 m. The geometry specification and open water propeller test results were published in [14, 15]. The main particulars of the propeller are given in Table 1 and its hydrodynamic coefficients are depicted in Fig. 5 in comparison with the numerical results of this study. The propeller geometry and coordinate system axes are shown in Fig. 1. The flow enters from the undisturbed side into the propeller disc. The X-axis is along the shaft

line opposite to the flow direction, the Z-axis is vertically upward and the Y-axis direction is according to the rule of the right-handed coordinate system, as depicted in Fig. 1(a). The inflow angle, β, is defined as the angle between the x-axis and the direction of free stream velocity. Here, β is specified in the x-y plane (see Fig. 1(b)).

Tab. 1. Main particulars of the DTMB-P4119 [15]

Diameter (m)	0.305
Number of blades	3
Hub ratio	0.2
Rotation	Right-handed

COMPUTATIONAL DOMAIN AND BOUNDARY CONDITION

The computational domain is a cubic volume having dimensions of $-6.5D \le x \le 4D$, $-5D \le y \le 5D$ and $-5D \le z \le 5D$, where D is the propeller diameter. The inlet and outlet are located at 4D and 6.5D upstream and downstream of the propeller plane, respectively. In addition, far-field walls are located at 5D from the propeller's centre axis. Fig. 2 shows the computational domain around the propeller and relevant boundary conditions (BC). At x = 4D and y = −5D, which are inlet boundaries, uniform velocity, k, and ω as well as a zero gradient of pressure are imposed. At x = −6.5D and y = 5D, which are outlet boundaries, the pressure is specified and the gradients of flow velocity, k and ω are set to zero. The no-slip boundary condition imposed on the propeller blades, hub and shaft, i.e. flow velocity, pressure gradients and turbulence quantities, are zero.

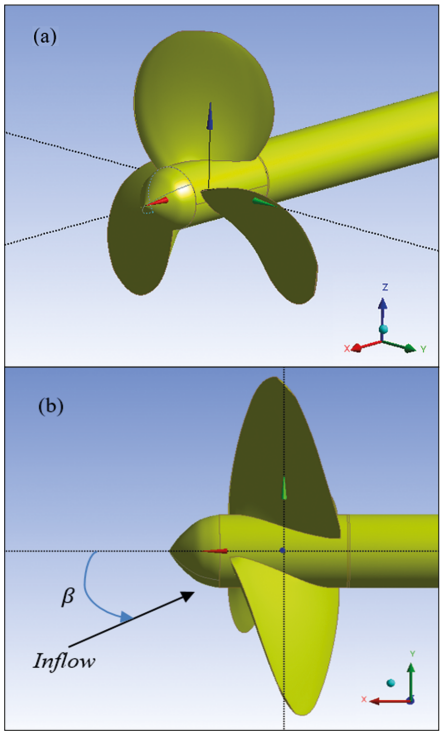

Fig. 1. Propeller geometry of DTMB-P4119 and oblique flow angle, (a) propeller geometry (b) inflow angle, β

In order to model the propeller rotation within the fluid, the sliding mesh method has been utilised. To use the method, the computational domain is divided into two parts, an outer fixed part and inner moving part. The inner part of the cylindrical shape surrounding the propeller can have rotational motion relative to the outer part as depicted in Fig. 3.

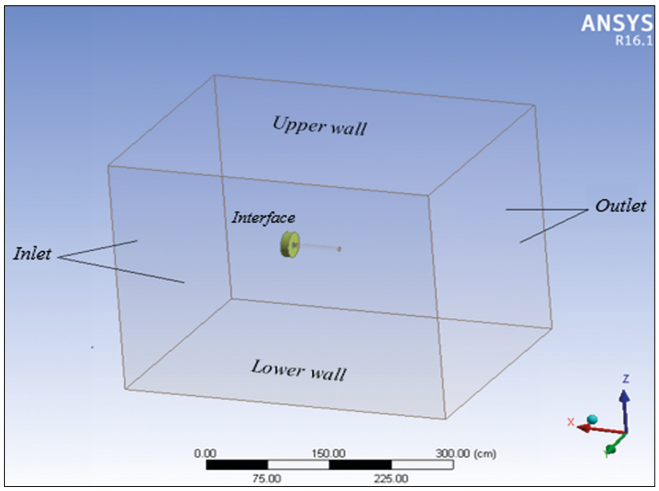

Fig. 2. Computational domain and relevant boundary conditions

At surfaces between fixed and moving parts, the interface boundary condition is imposed. In the interface boundary, two parts are connected through the interpolation of the flow data exchanged between the adjacent joint surfaces. Fig. 3 shows a view of the grid generated on the propeller. The inner part containing propeller and grid elements rotates at each time step during the simulations. The thick black circle in Fig. 3 distinguishes the sliding surface that is the interface boundary.

COMPUTATIONAL GRID

Due to the complexity of the propeller geometry, an unstructured grid is generated to perform simulations. To capture the details of the flow, a high grid resolution has to be used near the propeller surface. The grid is composed of triangular prism layer meshes on the propeller surfaces, which is known as boundary layer mesh, and tetrahedral cells in the remaining spaces. For the grid generation, according to the wall treatment in the turbulence model, special attention should be given to the dimensionless distance from the wall (Y+). Based on the pre-calculation, the distance of the first grid to the wall is 0.2 mm, which results in an appropriate Y+ in the present simulations. The boundary layer mesh technique facilitates adjustment of the first grid distance from the wall, as well as preventing a significant increase of the number of cells. In order to study the mesh independency, three coarse, medium and fine grids are generated, which have roughly 1.1 million, 2.5 million and 4.2 million elements, respectively. Fig. 4 shows schemes of the medium grid in mid-plane of the propeller.

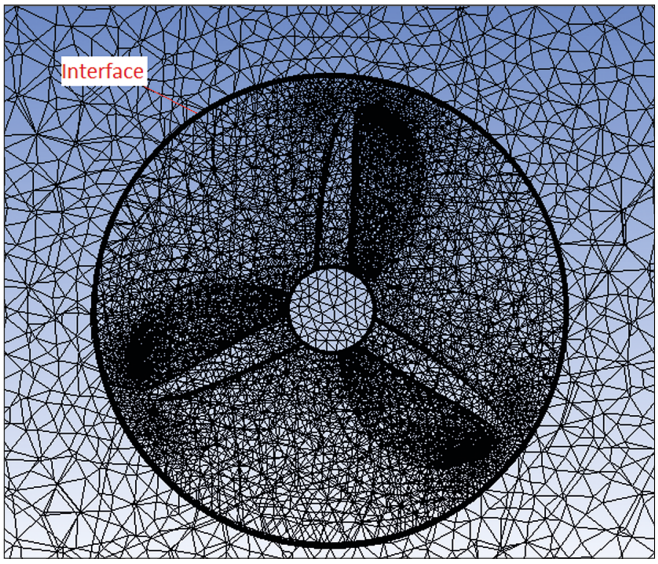

Fig. 3. Computational grid generated on the propeller plane and sliding surface

SOLVER SETTING, GRID AND TIME-STEP INDEPENDENCE STUDIES AND VALIDATION

SOLVER PARAMETERS SETTING

The settings of the solver parameters for the propeller open water simulations are given in Table 2.

GRID AND TIME-STEP INDEPENDENCE STUDIES

In order to obtain reliable numerical results, it is necessary to perform grid and time-step independence studies. For this purpose, numerical simulations are carried out on the coarse, medium and fine grids for two cases of J = 0.5 (n = 10 *rps*, U = 1.525 m/s) at a 30° inflow angle and J = 0.833 (n = 10 *rps*, U = 2.541 m/s) at a 10° inflow angle. The time-step size is chosen based on the number of time-steps (NS) in one propeller revolution. For the grid study, the time-step is fixed at 200 per revolution. To study the time-step independence, the number of time-steps in each propeller revolution is specified as 100, 200 and 400. Tables 3 to 6 show the results of the grid and the time-step independence studies.

As far as the grid independence study is concerned, comparison of the results of the fine and medium grid reveals that the discrepancy of the propeller force and moment coefficients is very small and they are not sensitive to the grid resolution. Except for the vertical force coefficient (K_{T_z}), which is probably due to the small absolute values, discrepancies in both advance coefficients are less than 3%. Therefore, the medium grid is chosen for subsequent calculations in this research. As far as the time-step independence study is concerned, by increasing the NS, the relative differences of the force coefficient are reduced. When NS reaches 200, the relative errors of the force and moment coefficients are approximately less than 3%. Therefore, it can be concluded that the effect of the time-step size on the numerical results is negligible. Thus, further calculations were conducted at NS equal to 200.

VALIDATION

To validate the numerical approach, the DTMB-P4119 model propeller was simulated in the open water condition for a range of advance coefficients in the axial flow condition. The thrust and torque coefficients and the efficiency are calculated using Eqs. (10), (11) and (12) respectively.

$$K_T = \frac{T}{\rho n^2 D^4} \tag{10}$$

$$K_Q = \frac{Q}{\rho n^2 D^5} \tag{11}$$

$$\eta_0 = \frac{K_T}{K_Q} \times \frac{J}{2\pi} \tag{12}$$

where T and Q are the thrust and torque, η_0 is the efficiency and n is the rate of revolution.

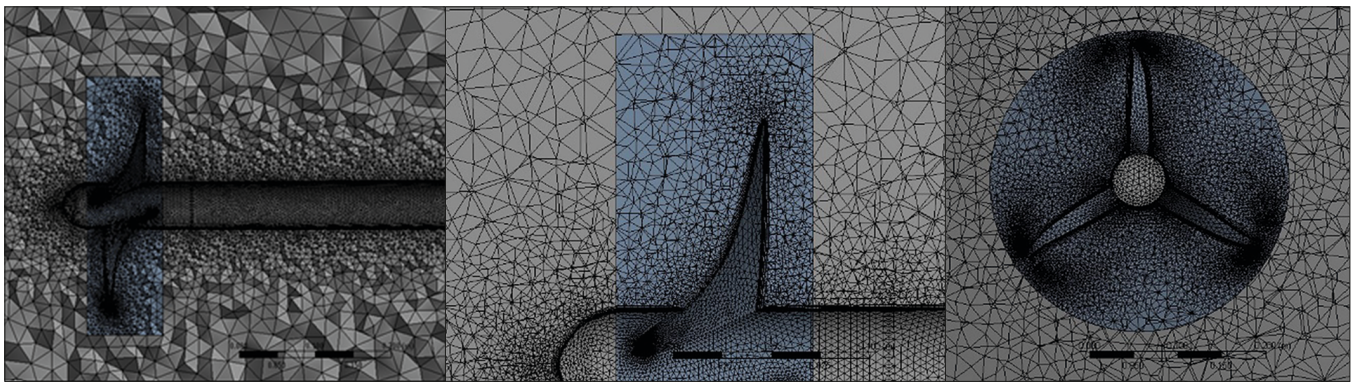

Fig. 4. Schemes of the medium grid in mid-plane of propeller

Tab. 2. Solver parameters setting

Parameter	Setting
Solver	3D, pressure-based, unsteady
Velocity formulation	Absolute
Viscous model	*k-ω* turbulent model
Wall model	Enhanced wall function
Gradient discretisation	Least squares cell-based
Pressure discretisation	Standard
Momentum discretisation	Second order upwind
Turbulent kinetic energy discretisation	Second order upwind
Turbulent dissipation rate discretisation	Second order upwind
Pressure–velocity coupling	SIMPLE

In Fig. 5, the calculated thrust and torque coefficients are compared with the experimental data presented by [14]. As can be seen, the curves trends are well predicted. However, the numerical results over-predict and the discrepancies increase with decrease of the advance coefficient. This might be due to the hard-to-conform experimental conditions in the numerical simulation. The relative error for various advance coefficients is given in Fig. 6. The maximum error is about 8% and 10% for the thrust and torque coefficients, respectively, which can be regarded as a fair agreement. Unfortunately, experimental results are not available for the propeller model under consideration in the oblique flow condition. Thus, the present numerical method set-up is utilised for oblique flow calculations regarded as a verified method.

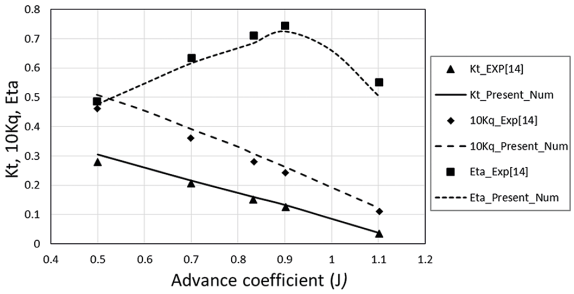

Fig. 5. Comparison of numerical and experimental thrust and torque coefficients

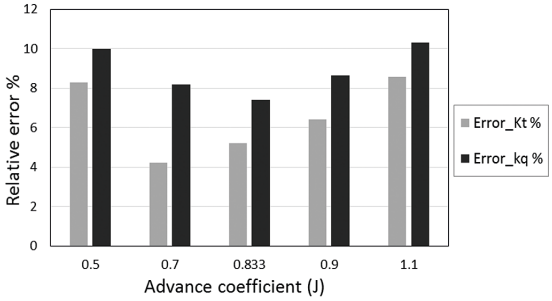

Fig. 6. The relative error of numerical results of thrust and torque coefficients

Tab. 3. Grid study for J = 0.833, β = 10° at time-step of 200 per revolution

Grid	KTx	Err%	KTy	Err%	KTz	Err%	10KQx	Err%	10KQy	Err%	10KQz	Err%
Coarse	0.157	3.09	0.0365	9.28	0.0059	11.9	0.335	2.39	0.107	2.88	0.0088	4.6
Medium	0.162	0.61	0.0334	1.52	0.0067	5.63	0.324	1.90	0.104	0.95	0.0093	1.06
Fine	0.163	--	0.0329	--	0.0071	--	0.315	--	0.105	--	0.0094	--

Tab. 4. Grid study for J = 0.5, β = 30° at time-step of 200 per revolution

Grid	KTx	Err%	KTy	Err%	KTz	Err%	10KQx	Err%	10KQy	Err%	10KQz	Err%
Coarse	0.311	3.75	0.0405	8.3	0.0272	14.19	0.519	2.99	0.232	3.11	0.0748	4.83
Medium	0.323	0.62	0.0374	2.18	0.0317	6.49	0.535	2.29	0.225	0.89	0.0786	1.00
Fine	0.325	--	0.0366	--	0.0339	--	0.523	--	0.223	--	0.0794	--

Tab. 5. Time-step study for J = 0.833, β = 10°, for medium grid

Grid	NS	KTx	Err%	KTy	Err%	KTz	Err%	10KQx	Err%	10KQy	Err%	10KQz	Err%
Medium	100	0.152	6.17	0.0316	5.39	0.0061	8.95	0.308	4.93	0.101	2.88	0.0096	3.22
Medium	200	0.162	2.41	0.0334	1.84	0.0067	2.89	0.324	2.99	0.104	1.89	0.0093	1.06
Medium	400	0.166	--	0.0340	--	0.0069	--	0.3334	--	0.106	--	0.0094	--

Tab. 6. Time-step study results for J = 0.5, β = 30°, for medium grid

Grid	NS	KTx	Err%	KTy	Err%	KTz	Err%	10KQx	Err%	10KQy	Err%	10KQz	Err%
Medium	100	0.301	6.81	0.0352	5.88	0.0287	9.46	0.505	5.61	0.218	3.11	0.0757	3.69
Medium	200	0.323	2.71	0.0374	2.09	0.0317	3.06	0.535	3.25	0.225	2.17	0.0786	1.50
Medium	400	0.332	--	0.0382	--	0.0327	--	0.553	--	0.230	--	0.0798	--

RESULTS AND ANALYSIS

RESULTS

For all calculations, the rotational speed of the propeller is set as $n = 10$ *rps*, and the free-stream velocity is specified for different advance coefficients according to J = U/nD. Fig. 7 presents the propeller hydrodynamic forces and moments versus the advance coefficient for a range of inflow angles. The forces and moments coefficients are defined as follows:

$$K_{T_i} = \frac{T_i}{\rho n^2 D^4} \tag{13}$$

$$K_{Q_i} = \frac{Q_i}{\rho n^2 D^5} \qquad i = x, y, z \tag{14}$$

The open water propeller efficiency is calculated by:

$$\eta_0 = \frac{K_{T_x}}{K_{Q_x}} \times \frac{J}{2\pi} \tag{15}$$

where $T_i = (T_x, T_y, T_z)$, where T_x, T_y and T_z are the forces in the x, y and z directions, respectively. $Q_i = (Q_x, Q_y, Q_z)$, where Q_x, Q_y and Q_z are the moments in the x, y and z directions, respectively. The coefficients shown in Fig. 7 are time-averaged values of forces and moments in one revolution calculated by the following equations.

$$\overline{K_{T_l}} = \frac{1}{\tau}\int_0^T K_{T_i} d\tau \tag{16}$$

$$\overline{K_{T_l}} = \frac{1}{\tau}\int_0^T K_{Q_i} d\tau \tag{17}$$

where τ is the time duration for one revolution, $d\tau$ is the time-step, $\overline{K_{T_l}}$ and $\overline{K_{Q_l}}$ are the time-averaged values of the force and moment coefficients, respectively. As can be seen in Fig. 7, the thrust and axial torque coefficients (K_{T_x}, K_{Q_x}) decrease as the advance coefficient increases. Increasing the inflow angle up to 10° results in no significant change to the coefficients. However, at high inflow angles, the thrust and torque coefficients get larger, and the change is more visible for the high advance ratios. The side force and moment coefficients (K_{T_y}, K_{Q_y}) become larger with increase of the advance ratio at non-zero inflow angles. Increasing the inflow angle will result in an increase of the side force and moment coefficients, and it is more pronounced as the advance coefficient becomes larger. The vertical force and moment coefficients (K_{T_z}, K_{Q_z}) are much smaller than the side force and moment coefficients. Increase of the advance ratio initially increases and finally decreases K_{T_z}. As expected, increase of the inflow angle increases K_{T_z}. Considering the inflow angle effect on K_{Q_z}, as the angle increases from zero to 30°, a small moment coefficient is generated. For a given inflow angle, K_{Q_z} changes its direction from up to down. The small K_{Q_z} values compared with K_{Q_y} are due to the oblique flow direction.

The open water characteristic curves of the propeller are depicted in Fig. 8 for different inflow angles. As can be seen, with increase of the inflow angle up to 10°, no appreciable change is observed in the propeller thrust and torque coefficients. However, at high inflow angles, the coefficients change considerably. The thrust (K_{T_x}) and torque (K_{Q_x}) increase by up to 42% and 22%, respectively, for the medium advance ratio (J = 0.88), and by up to 10% and 6% for the lower one (J = 0.5), respectively. An interesting result is that the propeller efficiency improves with increase of the inflow angle. As the angle increases, the peak of efficiency grows and it shifts to the higher advance coefficients. For instance, at the 30° inflow angle, the efficiency increases by about 15% relative to the zero angle.

ANALYSIS

To explain the numerical results at the inflow angle condition, velocity vectors for a blade section operating in oblique flow are plotted in Figs. 9 and 10. For this purpose, the velocities are projected in the reference frame moving with the blade. As can be seen, the inflow velocity consists of axial (u_α) and tangential (v_{tan}) components that are defined as below:

$$u_\alpha = U_\infty cos\beta \tag{18}$$

$$v_{tan} = v_\omega + v_\beta = \omega r - U_\infty sin\beta,\ sin\theta \tag{19}$$

where U_∞ is the free-stream velocity, θ is the blade angular position, ω is the propeller revolution rate and r is the radial position of the blade section. v_ω and v_β are tangential velocity components due to propeller rotation and transverse flow, respectively.

It is obvious that, for a given revolution rate and the oblique angle, u_α and v_ω remain constant, whereas v_β changes during a 360° propeller rotation. Consequently, according to Eq. (19), the tangential component of inflow into the blade section (v_{tan}) exhibits sinusoidal variations. Thus, the angle of attack of the inflow varies during propeller rotation. The angle of attack is defined as follows:

$$\alpha = \Phi - arctan\ \frac{u_\alpha}{v_{tan}} \tag{20}$$

where Φ is the geometric pitch angle of the blade section. In order to examine the effects of the transverse flow component on the blade hydrodynamics, velocity vectors for a blade section are sketched in Fig. 9 in two different angular positions (θ_1 and θ_2). In the θ_1 position, v_ω and v_β are in opposite directions while in the position, they have the same direction. Therefore, in the θ_1 position, the angle of attack reduces and in the θ_2 position it increases with

respect to pure axial flow. Consequently, for the oblique flow condition, time-dependent blade loads during the propeller rotation result in the generation of time-varying forces and moments in the propeller-plane.

The variations of blade forces and moments during one propeller rotation are presented in Fig. 11 for J = 0.833 at a 10° inflow angle. Fluctuation of blade loads shown in Fig. 11 is due to oscillatory (harmonic) variation of the flow angle of attack. As illustrated, during the blade movement in the lower half of the propeller disc ($180 < \theta < 360$), the thrust and side force coefficients have larger values than the upper half ($0 < \theta < 180$) and their maximum values occur around $\theta = 270°$. It is interesting to know that, although there is no vertical velocity component in the inflow, the mean value of the vertical force (which is much smaller than the side force) is not zero. That is due to the non-uniform distribution of the induced velocity in the propeller disc [5, 11].

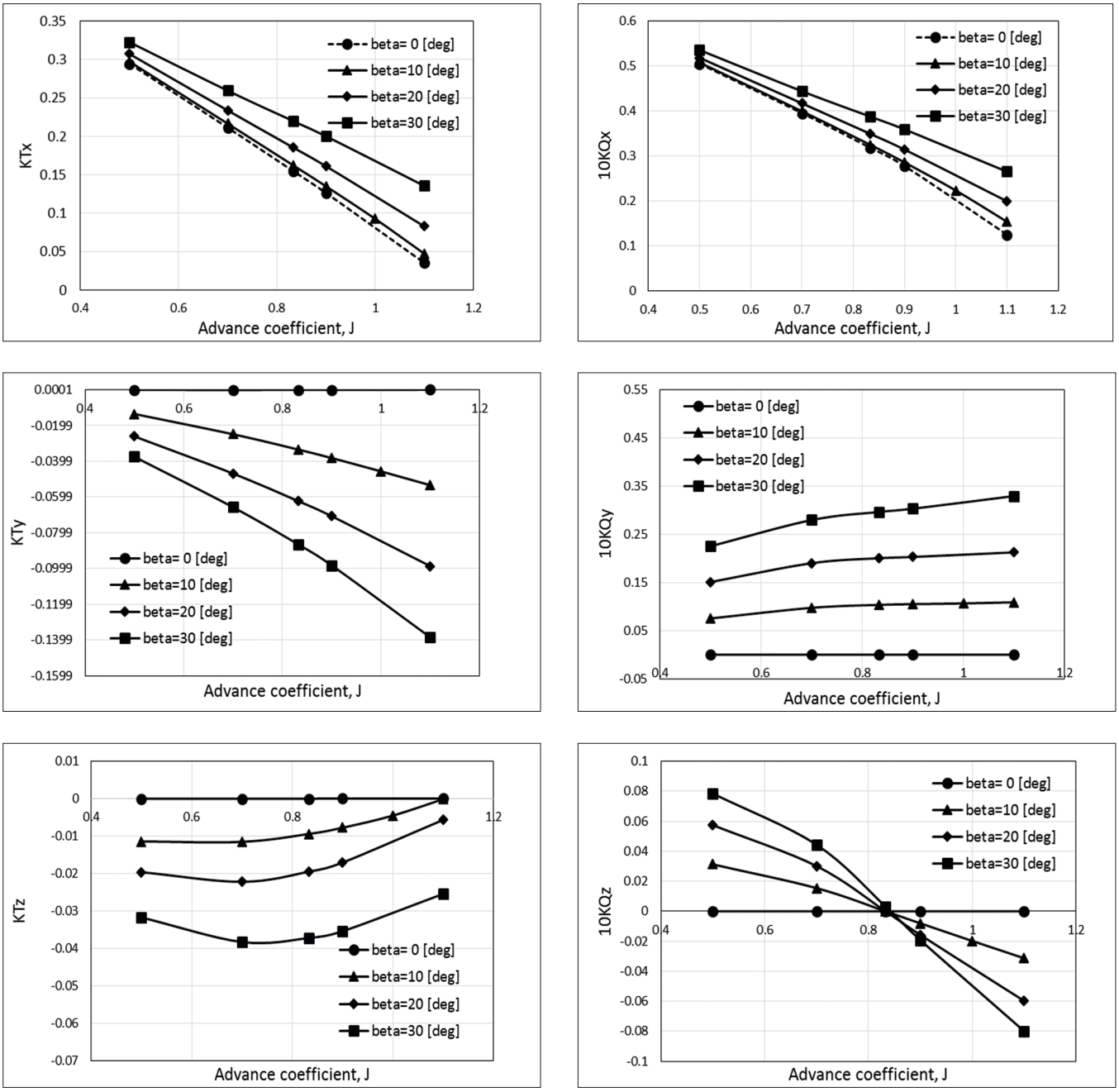

Fig. 7. Hydrodynamic force and moment of propeller versus J for different inflow angles

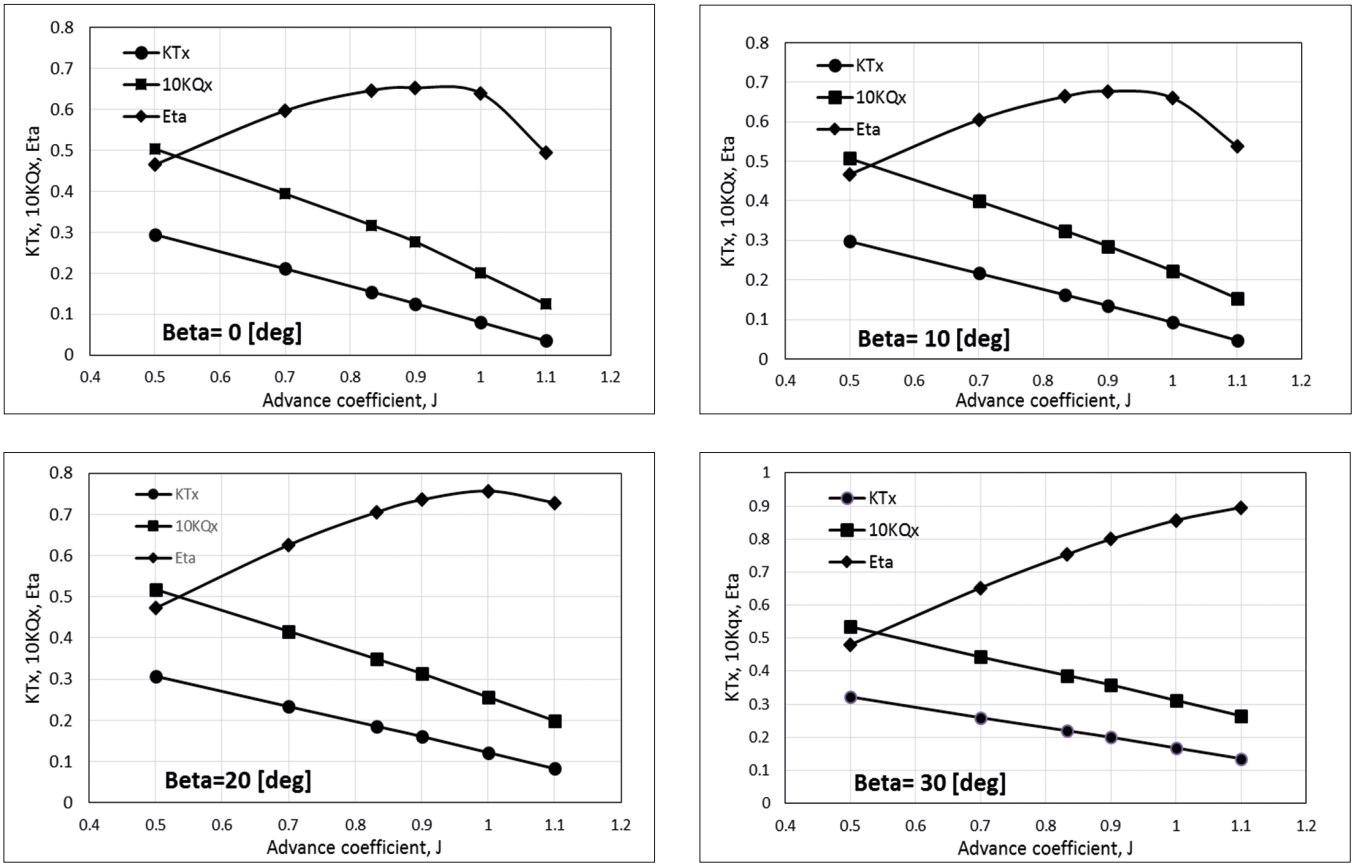

Fig. 8. Propeller open water characteristic curves for different inflow angles

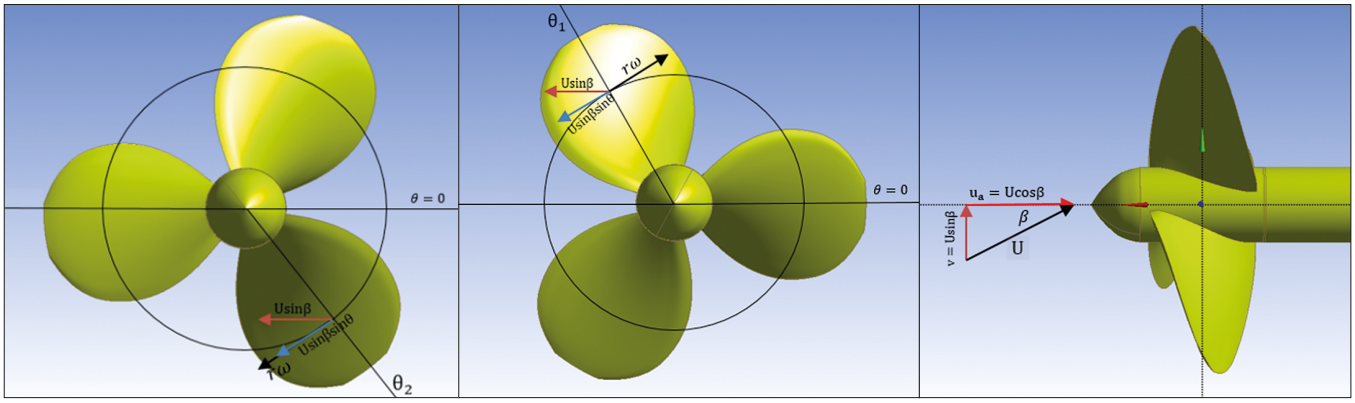

Fig. 9. Velocity components in propeller plane in oblique flow condition

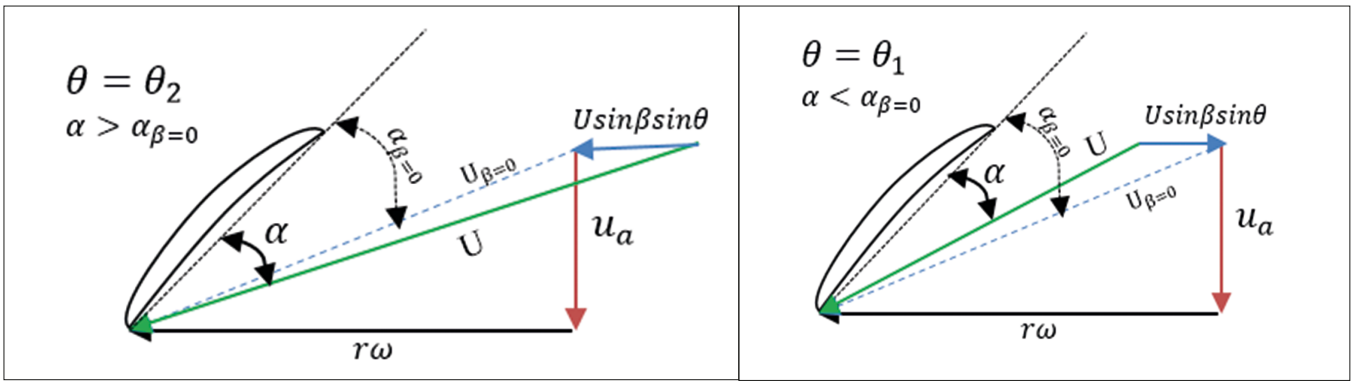

Fig. 10. Blade section velocity vectors for oblique flow condition in two different angular positions [11]

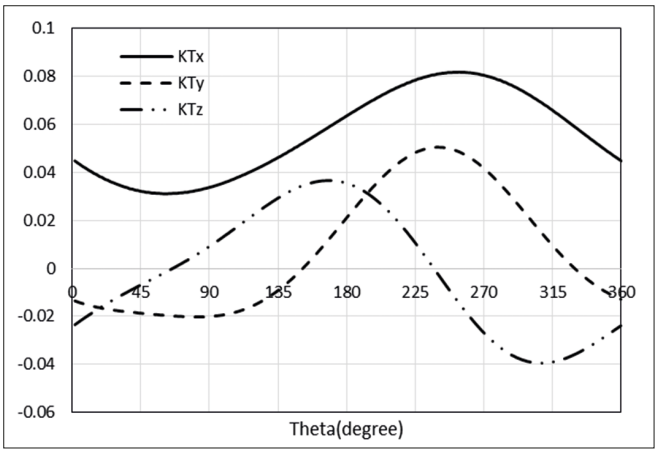

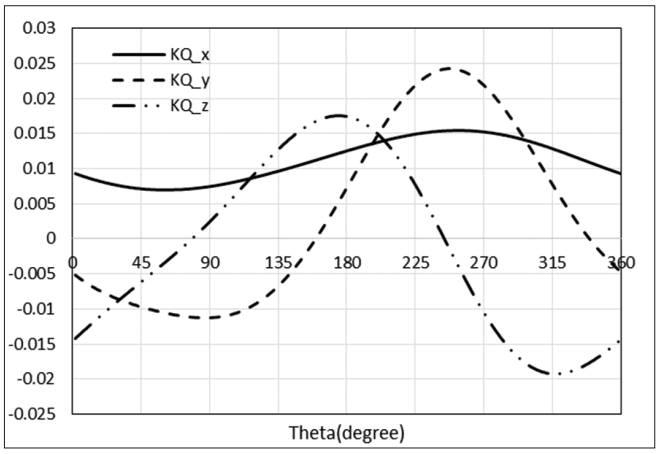

Fig. 11. Blade force and moment coefficients variations during one propeller revolution for J = 0.833, β = 10°

CONCLUSION

The main intention of the present study is to evaluate the effect of the inflow angle on the hydrodynamic characteristics of a propeller using an unsteady RANS equation. The sliding mesh technique is employed to simulate the propeller's rotational motion. The numerical results have been validated by experimental data at a zero inflow angle. From the studied case, the following conclusions can be drawn: -

- Small inflow angles such as 10° or less may have no significant influence on the thrust and torque coefficients or propeller efficiency. At high inflow angles, the thrust and torque coefficients may increase, which results in a considerable improvement of propeller efficiency for the studied case. For instance, at a 30° inflow angle, the propeller efficiency improved by up to 15%.
- Transverse and vertical forces and moments are developed at non-zero inflow angles, where the vertical components are much smaller than the transverse components. Increasing the inflow angle increases the transverse and vertical loads. The influence of the inflow angle is more pronounced at high advance coefficients.
- The blade's force and moment during one propeller rotation result in the generation of time-dependent forces and moments, which is due to the oscillatory nature of the flow angle of attack.
- The results show a gain of propeller efficiency at high inflow angles, which can potentially be utilised as a tool for reducing ship fuel consumption. At the same time, it develops excessive lateral loads on the ship stern, which should be considered in structural design. The lateral loads must be also included in the ship steering system.

This study may be pursued further to investigate the propeller shaft angle in the propeller design.

REFERENCES

1. Abbasi A., Ghassemi H., Fadavie M. (2018): *Hydrodynamic Characteristic of the Marine Propeller in the Oblique Flow with Various Current Angle by CFD Solver*. American Journal of Marine Science, 6(1), 25–29.

2. Atsavapranee P. (2010): *Steady-turning experiments and RANS simulations on a surface combatant hull form (Model# 5617)*. 28th Symposium on Naval Hydrodynamics, Pasadena, 2010.

3. Broglia R., Dubbioso G., Durante D., Di Mascio A. (2013): *Simulation of turning circle by CFD: Analysis of different propeller models and their effect on maneuvering prediction*. Applied Ocean Research, 39, 1–10.

4. Chase N., Carrica P. M. (2013): *Submarine propeller computations and application to self-propulsion of DARPA Suboff*. Ocean Engineering, 60, 68–80.

5. Coleman R. P., Feingold A. M., Stempin C. W. (1945): *Evaluation of the induced-velocity field of an idealized helicopter rotor.* National Aeronautics and Space Administration, Hampton, VA; Langley Research Center.

6. Coraddu A., Dubbioso G., Mauro S., Viviani M. (2013): *Analysis of twin-screw ships' asymmetric propeller behavior by means of free running model tests*. Ocean Engineering, 68, 47–64.

7. Dubbioso G., Durante D., Broglia R., Mauro S. (2012): *Comparison of experimental and CFD results for a tanker-like vessel*. Proceedings of MARSIM, 2012.

8. Dubbioso G., Muscari R., Di Mascio A. (2013): *Analysis of the performances of a marine propeller operating in oblique flow*. Computers & Fluids, 75, 86–102.

9. Dubbioso G., Muscari R., Di Mascio A. (2014): *Analysis of a marine propeller operating in oblique flow. Part 2: very high incidence angles*. Computers & Fluids, 92, 56–81.

10. Dubbioso G., Muscari R., Ortolani F., Di Mascio A. (2017): *Analysis of propeller bearing loads by CFD. Part I: straight ahead and steady turning maneuvers*. Ocean Engineering, 130, 241–259.

11. Dubbioso G., Muscari R., Di Mascio A., eds. (2013): *CFD analysis of propeller performance in oblique flow*. 3rd International Symposium on Marine Propulsors, SMP, 2013.

12. Durante D., Broglia R., Muscari R., Di Mascio A. (2010): *Numerical simulations of a turning circle maneuver or a fully appended hull*. 28th Symposium on Naval Hydrodynamics, Pasadena, CA.

13. Hochbaum A. C. (2006): *Virtual PMM tests for maneuvering prediction*. 26th Symposium on Naval Hydrodynamics, Rome, Italy.

14. Jessup S. (1998): *Experimental Data for RANS Calculations and Comparisons (DTMB P4119)*. 22nd ITTC Propulsion Committee Propeller RANS. Panel Method Workshop, Grenoble.

15. Koyama K. (1993): *Comparative calculations of propellers by surface panel method*. Workshop organized by 20th ITTC Propulsor Committee. Ship Research Institute, Supplement, 1993 (15).

16. Krasilnikov V., Zhang Z., Hong F., eds. (2009): *Analysis of unsteady propeller blade forces by RANS*. 1st International Symposium on Marine Propulsors (SMP), Trondheim, Norway, June, 2009.

17. Menter F. R., Kuntz M., Langtry R. (2003): *Ten years of industrial experience with the SST turbulence model*. Turbulence, Heat and Mass Transfer, 4(1), 625–32.

18. Nakisa M., Abbasi M. J., Amini A. M. (2010): *Assessment of marine propeller hydrodynamic performance in open water via CFD*. Proceedings of 7th International Conference on Marine Technology (MARTEC 2010),Dec. 2010.

19. Ortolani F., Mauro S., Dubbioso G. (2015): *Investigation of the radial bearing force developed during actual ship operations. Part 1: Straight ahead sailing and turning maneuvers.* Ocean Engineering, 94, 67–87.

20. Ortolani F., Mauro S., Dubbioso G. (2015): *Investigation of the radial bearing force developed during actual ship operations. Part 2: Unsteady maneuvers*. Ocean Engineering, 106, 424–45.

21. Rhee S. H., Joshi S. (2005): *Computational validation for flow around a marine propeller using unstructured mesh based Navier-Stokes solver*. JSME International Journal, Series B, Fluids and Thermal Engineering, 48(3), 562–70.

22. Ribner H. S. (1945): *Propellers in yaw*. NACA.

23. Shamsi R., Ghassemi H. (2017): *Determining the Hydrodynamic Loads of the Marine Propeller Forces in Oblique Flow and Off-Design Condition*. Iranian Journal of Science and Technology, Transactions of Mechanical Engineering, 41(2), 121–7.

24. Shamsi R., Ghassemi H. (2013): *Numerical investigation of yaw angle effects on propulsive characteristics of podded propulsors*. International Journal of Naval Architecture and Ocean Engineering, 5(2), 287–301.

25. Simonsen C. D., Otzen J. F., Klimt C., Larsen N. L., Stern F., eds. (2012): *Maneuvering predictions in the early design phase, using CFD generated PMM data*. 29th Symposium on Naval Hydrodynamics.

26. Viviani M., Podenzana Bonvino C., Mauro S., Cerruti M., Guadalupi D., Menna A. (2007): *Analysis of asymmetrical shaft power increase during tight maneuvers*. 9th International Conference on Fast Sea Transportation (FAST2007), Shanghai, China, 2007.

27. Wilcox D. C. (1998): *Turbulence modeling for CFD*. DCW Industries, La Canada, CA.

28. Yao J. (2015): *Investigation on hydrodynamic performance of a marine propeller in oblique flow by RANS computations*. International Journal of Naval Architecture and Ocean Engineering, 7(1), 56–69.

CONTACT WITH The AUTHORS

Hossein Nouroozi
e-mail: h.nouroozi@aut.ac.ir

Amirkabir University of Technology
Hafez, 15875-4413 Tehran
Iran

Hamid Zeraatgar
e-mail: hamidz@aut.ac.ir

Amirkabir University of Technology
Hafez, 15875-4413 Tehran
Iran